# Extensive characterization of Marshak waves observed at the LIL laser facility

C Courtois, O Breton, S Darbon, J Fariaut, O Henry, D Raffestin, C Reverdin, G Soullie, B Villette

# Extensive characterization of Marshak waves observed at the LIL laser facility

C. Courtois,[1,a)] R. Gisbert,[1] O. Breton,[2] S. Darbon,[1] J. Fariaut,[1] O. Henry,[3] D. Raffestin,[3] C. Reverdin,[1] G. Soullie,[1] B. Villette[1]

[1]*CEA, DAM, DIF, F-91297 Arpajon, France*

[2]*CEA, DAM, VALDUC, F-21120 Is sur Tille, France*

[3]*CEA, DAM, CESTA, F-33114 Le Barp, France*

[a)]Author to whom correspondence should be addressed: cedric.courtois@cea.fr

We detail results of an experiment performed at the Ligne d'Intégration Laser (LIL) facility aimed at studying supersonic and diffusive radiation front propagation in low density $SiO_2$ aerogel (20 and 40 mg/cm$^3$) enclosed in a gold tube, driven by thermal emission from a laser-heated spherical gold cavity. Evolution of the front is studied continuously by measuring its self-emission with a 1D (1 dimensional) time resolved soft-x-ray imager. Measurement is performed along (through a 200 µm wide observation slit) and at the exit of the tube giving access to the dynamics and the curvature of the front. Experimental results are then compared successfully to results from the 3D (3 dimensional) radiation hydrodynamics code TROLL which shows that if continuous tracking of the front position is accessible with this experimental scheme, measurement of its maximum radiation temperature is on the contrary affected by radiation closure of the observation slit. 3D simulations also indicate that this effect can even be worsened if one includes pointing errors of the x-ray imager. Radiation temperature along the tube was then inferred by combining results from the imager to a wall shock breakout time measurement using a VISAR and results from a broadband x-ray spectrometer used to determine the temperature at the exit of the tube. A decrease of the radiation temperature along the tube is observed, the decrease being more important for the higher $SiO_2$ aerogel density.

## I. INTRODUCTION

Radiation transfer plays an important role in many high energy density plasmas such as those encountered in astrophysics but also those produced in the laboratory.[1,2] In the indirect drive configuration of Inertial Confinement Fusion (ICF) experiments for instance, high-power laser beams energy focused inside a gold hohlraum is converted into x-rays.[3] X-ray energy absorption inside the cavity wall and reemission, depending on wall albedo, set the radiation field in the hohlraum and the performances of the implosion of the capsule containing the deuterium–tritium (DT) fuel ultimately. At early time, the penetration of x-ray in the cavity wall can be assumed supersonic, that is fast enough so that heated material expansion is limited and wall density remains constant at its nominal value. Later on, cavity walls start to expand and the hydrodynamic motion affects the radiation front propagation. The transition time when x-ray propagation goes from supersonic to subsonic decreases with the material density (~ $\rho_0^{-1.92}$ for gold) and it is typically in the picosecond scale for gold at solid density.[4] That transition time can be considerably extended, typically to the ns scale, by using low density foam or aerogel material in order to experimentally study it.[5,6] A large number of laser plasma experiments dedicated to supersonic front study using low density material irradiated by soft x-ray source (photon energy < keV) have been performed over the last 25 years. [7-14]

When an incoming soft x-ray flux interacts with a low-density foam, most of x-ray energy is deposited in a thin layer and the material is rapidly ionized and heated, which in turn reduces the opacity of the foam relative to the incident radiation. To qualitatively describe the propagation of the radiation front, it is convenient to assume that the material Rosseland mean opacity, $\kappa$, internal energy, $e$, are function of its density, $\rho$, and temperature, $T$, so that they can be approximated by, $e = fT^{\beta}\rho^{-\mu}$ and $1/\kappa = gT^{\alpha}\rho^{-\lambda}$,[15] where, f ~ 8.77, $\beta$ ~ 1.1, $\mu$ ~ 0.09, g~1/9175, $\alpha$ ~ 3.53, $\lambda$ = 0.75 for $SiO_2$ aerogel used in this study.[16] As the aerogel opacity decreases when

the temperature increases, radiation propagates through the ionized material and is absorbed at the edge of the cold material producing a radiation front. If the aerogel density is low enough, the front propagates supersonically, and the heated material density can be assumed constant since it has not expanded yet. Supersonic front can then be characterized by a radiative Mach number $M(t)=\partial_t z_F(t)/c_0(t) > 1$ where $z_F$ and $c_0$ correspond to the front position and the sound velocity respectively. In a 1D approximation of the problem and if the drive temperature is constant, $z_F \sim [\sigma T_{S0}^4 t/(\rho_0^2 \kappa e)]^{1/2}$ where $T_{S0}$ is the incident x-ray drive temperature, $\sigma$ is the Stefan-Boltzmann constant and $\rho_0$ the initial foam density, showing the decrease of the front velocity with time, $\partial_t z_F(t) \sim t^{-1/2}$.[16] The time, $t_{HS}$ when $M(t_{HS}) = \partial_t z_F(t_{HS})/c_0(t_{HS}) = 1$ (HS stands for "hydrodynamically separated" and refers to the instant when the shock and the radiation front physically separate)[6] can be written $t_{SH} = 4\Gamma g \sigma T_{S0}^{4+\alpha-2\beta} \rho_0^{-2+2\mu-\lambda}/[(12+3\alpha) r (1-\mu) f^2]$ where $\Gamma = 2+3\omega+(10/3)\omega^2+(251/72)\omega^3$, $\omega = \beta/(4+\alpha)$, $\sigma = 1.03\times10^{-2}$ MJ/ns/cm$^2$, $\Gamma = 2.7$, $T_{S0}$ is expressed in heV and t is time in ns.[4] Another point of view is to introduce the maximum density, $\rho_{HS}$, above which $M < 1$ for a given constant drive temperature $T_{S0}$ and duration t, $\rho_{HS}(t) = [4\Gamma g \sigma/[(12+3\alpha) r (1-\mu) f^2 t]]^{1/(2-2\mu+\lambda)} T_{S0}^{(4-2\beta+\alpha)/(2-2\mu+\lambda)}$.[4] For $SiO_2$ aerogel, an input drive temperature on the foam of 135 eV and a duration of 3 ns [see Fig. 2 and Fig. 7(c)], one gets a maximum allowed density to remain just supersonic ($M > 1$) of $\rho_{HS} = 140$ mg/cm$^3$. Similarly, a minimum aerogel density, $\rho_{DA}(t) = [gf/(\sigma t)]^{1/(\mu+\lambda)} T_{S0}^{-(4-\alpha-\beta)/(\mu+\lambda)}$,[4] can be introduced for the diffusion-approximation to be valid, that is to assume that the x-ray photon mean free path, $\lambda_{mfp} = (\rho_0 \kappa)^{-1}$, is smaller than the typical temperature gradient length (DA as "diffusion approximation"). One gets in our conditions $\rho_{DA} = 20$ mg/cm$^3$. In the experiment presented in this paper, the $SiO_2$ aerogel density was chosen low on purpose, at $\rho_0 \sim 20$ mg/cm$^3$ and $\rho_0 \sim 40$ mg/cm$^3$, to make sure the radiation front is well supersonic ($M > 2$) even if the diffusion approximation is then less valid.

Several experimental techniques have been employed to characterize supersonic radiation front. One dimensional (1D) time resolved K-shell absorption spectroscopy can be used to infer absolute plasma temperature spatial profile at different times.[5] These techniques require the opacity of the low density material to be well known during data analysis,[17] and also requires several snapshots to get information on front dynamics. The latter can be studied in a more direct way by measuring its self-emission using a soft x-ray imager. When the imager points at the exit of the tube, it gives access to the time when the supersonic radiation front breaks through the edge of the aerogel, but also to information on its curvature, as the front propagates faster on-axis than near the walls.[9,11] This is attributed to 2D effects such as radiation energy losses at the wall tube because of its low albedo, $a$, but also plasma wall expansion at the entrance of the tube that reduces x-ray flux transfer from the hohlraum to the foam.[16,18] Using tubes of different lengths on several shots gives information on the front dynamics by measuring breaking through at different discrete times. Note that this type of measurement can be coupled to a broad-band x-ray spectrometer used to measure spatially integrated but time resolved absolute radiation front x-ray power.[13] Other experiments used an observation slit machined along the tube axis to study front propagation longitudinally.[12,13] Measurements are usually based on multi-channel, time-gated x-ray imagers from which several 2D images of the front self-emission are obtained on a single shot. The front dynamics is studied by measuring through the slit, the front position inside the tube at different discrete times. This type of measurement can be more constraining, for analytical models or numerical simulations describing supersonic front dynamics, as multiple observation times are obtained on a single shot, reducing the effect of statistical fluctuations from shot to shot. Yet, as this measurement is based on gated x-ray imagers constituted of micro-channel plates (up to 4 at best), the front dynamics is again studied from measurements performed at limited discrete times.[12,13] An alternative to continuously follow the propagation of the supersonic front along the foam is to replace the gated x-ray

imager by a x-ray streak camera. This scheme has already been tested in a past experiment,[19] but it was mainly used in a transonic and subsonic regime of x-ray propagation as simulated results show important density fluctuations at the front during measurement time. Furthermore, the foam was not enclosed in a tube.

In this paper, results of an experiment performed at the LIL facility on the propagation of a supersonic and moderately diffusive radiation front in a low density $SiO_2$ aerogel (~ 20 mg/cm$^3$ and ~ 40 mg/cm$^3$) enclosed in a gold tube are presented. It is driven by the thermal radiation produced in a laser-heated spherical gold cavity. The front position is directly studied using a 1D soft x-ray imager coupled to a streak camera, and a broad-band x-ray spectrometer used to infer the front temperature at the exit of the tube. It is also indirectly studied by looking at an ablation shock launched by the radiation front in the wall of the gold tube using a Velocity Interferometer System for Any Reflector (VISAR). Experimental results are then successfully compared to 3D hydrodynamic simulations using the TROLL code; comparisons never presented before for that regime to our knowledge. Experimental setup is presented in section II and experimental results in section III. Results from radiation hydrodynamic numerical simulations are presented in section IV before the conclusion.

## II. EXPERIMENTAL SETUP

The results reported here were gathered during experiments performed using the LIL facility[20] at the CEA/CESTA which was a 4-beam prototype for the Laser Mégajoule (LMJ). Fig. 1(a) represents the experimental setup. Laser pulse was $\tau_L$ = 3 ns with square shape containing $E_{laser}$ ~ 12 kJ laser energy at 3ω (0.35 µm). It was focused on target using gratings that produce quasi-Gaussian focal spot, around 700 µm diameter, smoothed by combining longitudinal spectral dispersion and phase plates. The experiment was performed in indirect drive configuration where a gold tube containing a low-density silicon aerogel ($SiO_2$) is

mounted on a mm scale gold spherical hohlraum, at 90° of the laser entrance hole (LEH). The tube is protected from the laser energy contained in the focal spot at large radius (beyond the LEH) using a cone mounted around the LEH.

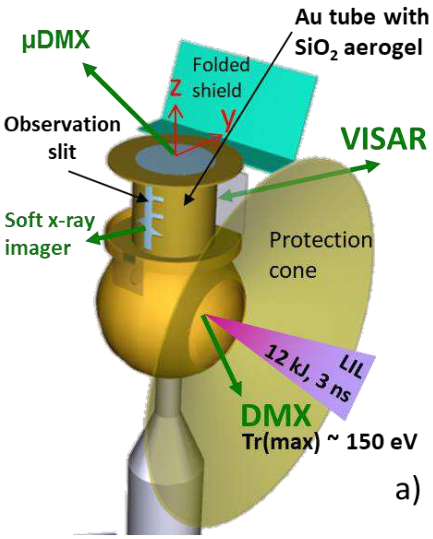


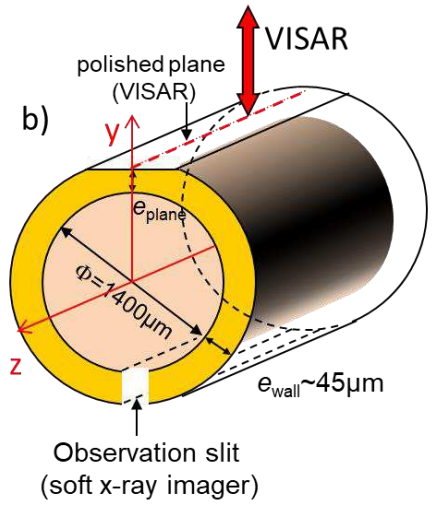

**FIG. 1.** (a) Experimental setup (configuration #1) showing the spherical cavity inside which the LIL laser beams are focused and the gold tube containing the $SiO_2$ aerogel. A protection cone and a folded shield are used to protect measurements from background noise. (b) Scheme of the gold tube showing the observation slit and the polished plane.

The $SiO_2$ aerogel has a cylindrical shape with a $\phi_{tube}$ = 1400 µm diameter and $L_{tube}$ = 1600 µm length for most of the shots (1500 µm for experimental configuration #2). Two aerogel densities were tested during this experiment, $\rho_0$ = 17.6±0.5 mg/cm$^3$ and $\rho_0$ = 39.4±1.2 mg/cm$^3$ chosen low enough to reach a supersonic regime of radiation front while keeping the optical depth above 1. A thin glint made of aluminized mylar ($e_{Al}$ = 50 nm, $e_{Mylar}$ = 100 nm) was mounted at the entrance of the gold tube to protect the aerogel against potential UV heating from the laser. The thickness of the gold tube was $e_{wall}$ = 45 µm except in the direction of the VISAR axis where it was reduced to $e_{plane}$ = 10±3 µm (or 30±3 µm depending on the target) as a polished plane was machined along the tube to improve the VISAR laser probe reflectivity [see Fig. 1(b)]. The plane normal is aligned along the VISAR probe axis. A 200 µm wide, 1400 µm long observation slit was also machined on the gold tube, opposite to the polished plane, to measure the self-emission of the radiation front propagating in the $SiO_2$ aerogel with the 1D soft x-ray imager. This slit starts at 100 µm from the beginning of the aerogel. Small transverse slits were machined along the main slit to help adjust the pointing of the soft x-ray imager. The z direction corresponds to the tube axis and position 0 to the beginning of the aerogel. The y direction is at 90° to the z direction and to the LEH normal, that is along the polished plane normal.

Radiation temperature history in the spherical gold cavity was inferred from the time-resolved broadband x-ray spectrometer DMX[21] which measures the x-ray emission from the LEH. DMX is set up with 20 channels. The first twelve use transmission filters and mirrors to select the soft part of the spectrum (< 1 keV). The eight following channels using transmission

filters only are dedicated to the hard part of the x-ray spectrum (> 1 keV). On Fig. 1(a) the tube is vertical, pointing toward the angular position (0°,0°) of the experimental chamber (configuration #1). The LEH normal is then along (90°,0°) and since DMX is located at (68°,18°), the angle between the LEH normal and DMX line of sight is then $\theta = 28°$. A miniaturized version of DMX called µDMX (comprising only 6 channels) located at (36°,144°) was also used to measure the time evolution of the radiation front temperature at the exit of the tube. Because of the large protection cone and its location on the experimental chamber, µDMX only measures x-ray signal from the exit of the tube and no emission coming from the LEH or the observation slit. The angle between the tube axis and µDMX line of sight is 36°.

A bi-mirror 1 dimensional soft x-ray imager located at (90°,270°) was used to measure self-emission from the supersonic radiation front through the observation slit.[22] These mirrors are coupled to a streak camera so that front emission can be continuously observed along the tube axis. For some of the laser shots, the target was rotated around the LEH normal with the gold tube axis pointing toward (90°,270°) instead of (0°,0°). In this configuration #2, the soft x-ray imager now measures the supersonic radiation front breaking through the edge of the aerogel.

Finally, a Velocity Interferometer System for Any Reflector (VISAR)[23-26] located at (90°,90°) was used (only for configuration #1) to study the wall breakout of ablation shocks launched by the radiation front inside the tube. In this configuration, the VISAR laser probe initially reflects on the polished plane of the tube and static interference fringes are obtained on VISAR images. When the ablation shock breaks out from the plane, fringes suddenly disappear because of gold wall reflectivity loss, giving indirectly access to information on the propagation of the radiation front. From this measurement, the propagation time of the shock through the $e_{plane}$ = 10 µm (or 30 µm) gold wall is measured to constrain numerical simulation of the

experiment. A folded shield was used at the exit of the tube to protect the VISAR from the intense emission from the radiation front when it reaches the exit of the tube.

To summarize, in configuration #1, the gold tube points towards the (0°,0°) direction, the propagation of the radiation front is directly studied along the tube using the soft x-ray imager and indirectly via the shock breakout measurement using the VISAR. The broad-band x-ray spectrometer μDMX absolutely measures the supersonic front temperature at the exit of the tube [see Fig. 1(a)]. In configuration #2, the tube points toward (90°,270°) and the soft x-ray imager is used to measure the front curvature and time to break through the edge of the aerogel at the exit of the tube. The radiation temperature of the cavity is inferred for all the shots using the broad-band x-ray spectrometer DMX.

## III. EXPERIMENTAL RESULTS

### A. CAVITY RADIATION TEMPERATURE

Figure 2 represents the cavity radiation temperature history inferred from DMX measurement for shot #2. The measured maximum temperature is between 152±3 and 157±3 eV for all shots.

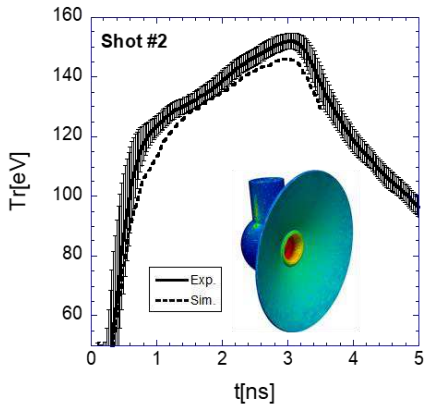

**FIG. 2.** Radiation temperature of the gold spherical cavity inferred from DMX measurement (solid line) and from TROLL numerical simulations (dotted line) for shot #2 ($\rho_0$ = 17.6 mg/cm$^3$ of $SiO_2$). The enclosed image is a view of the target radiation temperature from the TROLL simulations.

### B. DYNAMICS OF THE SUPERSONIC RADIATION FRONT

The soft x-ray imager is filtered with a thin Ti foil. Knowing the energy response of the streak camera, x-ray emission of the front is measured in the [200 eV - 450 eV] photon energy range. The images presented in this section are obtained after taking the ¼ power of the intensity data so that they are proportional to radiation temperature as black body emission is assumed. The time origin is defined relative to the laser pulse rising edge.

#### i. Measurement at the exit of the tube

Figure 3(a) shows an example of image obtained with configuration #2 when the imager points to the exit of the tube. As already shown by past experiments,[9,11,27] the front exhibits a curvature due to faster on-axis x-ray propagation than near the wall attributed to x-ray energy loss at the tube wall due to limited albedo, $a < 1$.[18]

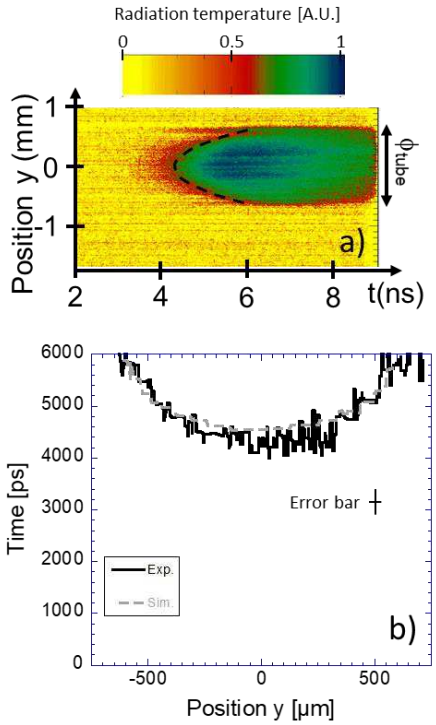


**FIG. 3.** (a) Results from the 1D soft x-ray imager showing the supersonic radiation front self-emission seen at the exit of the tube as a function of time for a $SiO_2$ aerogel at a density of $\rho_0 = 17.6$ mg/cm$^3$. (b) Measured (black solid line) and simulated (gray dotted line) transit time of the supersonic radiation front at the exit of a 1500 µm long gold tube as a function of the transverse y position ($\rho_0 = 17.6$ mg/cm$^3$, configuration #2). The cross shows the representative time and space error bar. The dashed line on Fig. 3(a) is a quadratic fit of the measured transit time plotted on Fig. 3(b).

From this type of images, temporal profiles can be extracted at different y positions along the tube diameter. The front transit time at a given position y is defined from these profiles at the inflection point of the rising front. Figure 3(b) is obtained after analyzing Fig. 3(a) and shows

the transit time at the exit of a 1500 µm long gold tube filled with 17.6 mg/cm$^3$ $SiO_2$ aerogel (black solid line). The front breaks through the edge of the aerogel at 4.3±0.25 ns on the tube axis (y = 0). The dashed line on Fig. 3(a) represents a quadratic fit of the measured transit time. This figure also shows a weak x-ray emission, that starts almost 1 ns ahead of this front, which is attributed to radiative precursors.

### ii. Measurement along the tube

Figure 4(a) shows an example of image obtained in configuration #1 when the imager points to the slit along the tube for an aerogel density of $\rho_0$ = 17.6 mg/cm$^3$. The self-emission of the supersonic front can be seen along the entire length of the slit (1400 µm). As a reminder, the observation slit starts at 100 µm from the beginning of the aerogel. Note the decrease of the signal strength around the position z = 100 µm as time goes by. This is attributed to the radiation closure of the observation slit, the expanding gold wall from the edge of the slit absorbing part of the radiation front self-emission [see section IV-A and Figure 11]. From these images, temporal profiles [see Fig. 5] can be extracted at different positions z along the tube. Again, the front transit time at a given position z is defined from these profiles at the inflection point. Figure 4(b) is obtained after analyzing images similar to the one presented on Fig. 4(a) and shows the transit time as a function of the longitudinal position z for two aerogel densities. An example of image obtained with the soft x-ray imager for $\rho_0$ = 39.4 mg/cm$^3$ is added. This inset image shows that the radiation front cannot be followed along the entire length of the observation slit, contrary to the low-density case [see Fig. 4(a)]. This difference is attributed to the slower propagation of the radiation front and consequently its weaker self-emission towards the end of the slit (z > 800 µm) as at that time (t > 4 ns) laser beams are off and the radiation temperature of the cavity is decreasing.

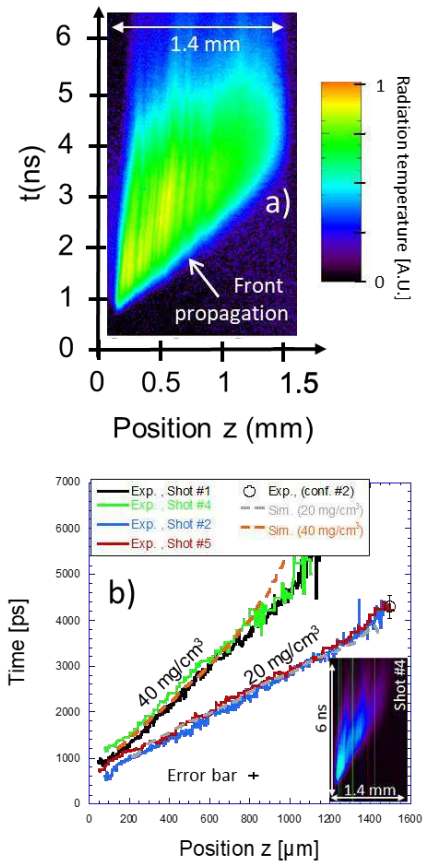


**FIG. 4.** (a) Results from the 1D soft x-ray imager showing the supersonic radiation front self-emission seen along the tube axis through the observation slit for a $SiO_2$ aerogel at a density of $\rho_0 = 17.6$ mg/cm$^3$ . (b) Transit time of the supersonic radiation front as a function of the longitudinal z direction along the tube (configuration #1) for two aerogel densities. The cross shows the representative time and space error bar. The experimental point at z = 1500 µm (label "Exp., (conf. #2)") is inferred from Fig. 3(b). The inset image is an example of result obtained with the soft x-ray imager for $\rho_0 = 39.4$ mg/cm$^3$. Solid and dashed lines correspond to experimental and numerical results respectively.

As expected, propagation velocity around $\partial_{tZF\_20mg/cc}$ ~ 410 km/s for $\rho_0$ = 17.6 mg/cm$^3$ and $\partial_{tZF\_40mg/cc}$ ~ 240 km/s for $\rho_0$ = 39.4 mg/cm$^3$ is faster at lower density. Radiation front propagation is here relatively linear with time and very reproducible from shot to shot. The time evolution of the model, $\partial_{tZF}(t) \sim t^{-1/2}$, given in the introduction is not found here as this 1D model assumes a constant drive temperature whereas it is increasing with time in this LIL experiment [see Fig. 2]. The model described in section III.D takes into account a time evolution of the radiation temperature to determine the radiation front position $Z_F$ [see Eq. (7)] and manage to reproduce results from Fig. 4(b) [see Fig. 9(a)]. Equation (4) of reference [16] is another expression of the radiation front position for a given time history of the drive radiation temperature. Assuming it can be written $T_r = T_{S0}(t/t_0)^{\delta}$, this Eq. (4) becomes $Z_F \sim t^{[1+\delta(4+\alpha-\beta)]/2}$ where as a reminder, $\alpha$ = 3.53 and $\beta$ = 1.1 for silicon aerogel. This expression shows as expected that for a constant drive temperature ($\delta$ = 0), $Z_F \sim t^{1/2}$ and that a time linear evolution is obtained for $\delta$ = 1/(4+$\alpha$-$\beta$) = 0.155 here. As shown in section III.D, the linear behavior is actually obtained for higher values of the parameter $\delta$. As explained in reference [16], this is due to several phenomena that tend to slow down the radiation front, such as energy losses to the walls and wall ablation, that have to be taken into account to improve this Eq (4).

Results from Fig. (4) show the interest of using a streak camera instead of a gated x-ray imager to continuously follow the front dynamics. The experimental transit time (from Fig. 3(b) at y = 0) obtained at z = 1500 µm in configuration #2 is consistent with those obtained in configuration #1. Thus, on-axis x-ray emission of the radiation front seems to be accessible from this side-on measurement (configuration #1) although the front is curved. This is likely due to the radiative precursors that extends ahead of the front over ~ 400 µm (x-ray emission from the precursors starts almost 1 ns ahead and $\partial_{tZF\_20mg/cc}$ ~ 410 km/s) [see Fig. 3(a)]. TROLL simulations show

indeed that in this region, x-ray photon mean free path is large enough for the on-axis front x-ray emission to be collected by the side-on measurement.

Figure 5 (a) and (b) show temporal profiles at different longitudinal positions z along the tube for two shots performed with the same cavity radiation temperature and $SiO_2$ aerogel density, $\rho_0$ = 39.4 mg/cm$^3$ (shots #1 and #4). If results from Fig. 4 (b) indicate that the front dynamics are very close between these two shots, the maximum of the temporal profiles exhibits a different behavior. Because of x-ray energy losses in the gold wall but also to ionize and heat the $SiO_2$ aerogel, the radiation temperature along the tube necessarily decreases with the longitudinal position z as shown by the evolution of the profile maxima. Yet the decrease rate is not the same between these two shots; a factor of 2 is observed over 700 µm for shot #1 and a factor of 4 for shot #4. As discussed in Sec. IV, this is mainly due to radiation closure of the observation slit combined to uncertainties on the pointing of the soft x-ray imager that prevents it from catching the peak temperature of the temporal profiles. If the use of a streak camera is useful to get access to a continuous track of the front position, maximum emission can be on the contrary affected by radiation closure. The observation slit surface corresponds here to ~ 4 % of the gold tube surface so that x-ray leaks through the slit has little impact on front dynamics (delay within 50 ps at the exit of the tube according to TROLL simulations). Taking into account this aspect, the use of a larger slit width should reduce the effect of radiation closure on radiation front temperature measurement.

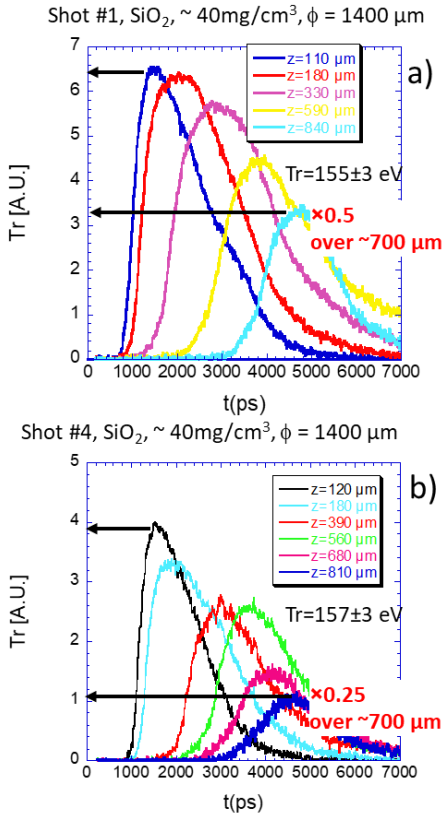


**FIG. 5.** Radiation temperature temporal profiles at different positions z along the tube for two shots performed with the same cavity radiation temperature and aerogel density ($\rho_0$ = 39.4 mg/cm$^3$). Fig. 5(b) profiles are extracted from the inset image of Fig 4(b).

### C. DECREASE OF THE FRONT TEMPERATURE ALONG THE TUBE

The radiation front temperature inside the gold tube was then indirectly assessed from a shock breakthrough measurement using the LIL VISAR. The radiation front inside the tube launches an ablation shock that propagates through the gold tube wall at a velocity, $V_{Au}$. The high-Z wall is here exposed to the front radiation temperature, $T_r$, the x-ray emission absorbed

by the wall producing an ablative shock wave ultimately. When this shock breaks out, the VISAR laser probe that was reflecting initially on the polish plane is no longer reflected by it and the VISAR interference fringes disappear. Since the VISAR is a 1D time resolved measurement, the fringe disappearance occurs first at the entrance of the tube and then is delayed as the position z increases because of the dynamics of the radiation front inside the tube [see Fig. 6 (a)]. The shock launched in the Au wall due to the radiation front is called here the "main shock". Preheating effect due to hard x-rays (~ kev) produced inside the gold cavity [see the scheme of the target on Fig. 6(b)] can also be at the origin of an energy deposition inside the gold wall (no preheating of the aerogel as its density is too low for keV photons to significantly deposit energy) which eventually also launches a second shock called here the "preheat shock". This shock is weaker than the "main shock" and does only modify here the VISAR probe intensity (lower wall reflectivity), without disappearance of the interference fringes. Since the "preheat shock" is due to hard x-rays from the cavity, it pushes on the tube wall earlier than the "main shock" governed by the supersonic front dynamics. At the entrance of the tube, the two shocks coalesce quickly within the wall, and a single shock breakout is observed. As the position z increases, the "preheat shock" is launched earlier and earlier compared to the "main shock" and eventually manages to breakout from the gold wall before the coalescence occurs. At that time, a reflectivity change is observed on the VISAR images without fringe disappearance. Consequently, the duration of the period of weaker fringes, corresponding to the delay between the "preheat shock" and the "main shock" breakout, increases with the position z. This is true for wall thickness small enough ($e_{\text{plane}}$ = 10 µm here) so that the "preheat shock" is not caught by the "main shock" before the breakout. As it was not completely sure how the VISAR reflectivity would behave with the breakout of the "preheat shock", some of the targets used thicker wall, 30 µm, in this experiment so that shocks necessarily coalesce within the tube wall before the breakout. Figure 6(b) show an example of

VISAR image obtained in the case of a $e_{plane}$ = 10 µm thick wall where the change of reflectivity of the VISAR probe due to the "preheat shock" and the fringe disappearance due to the "main shock" breakout can be observed. The fringe that lasts longer than the others on the image is due to VISAR laser probe reflection off a spatial fiducial.

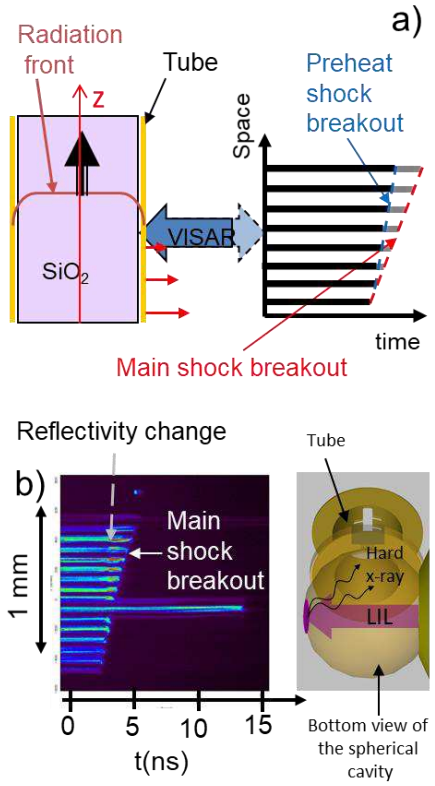


**FIG. 6.** a) Principle of the shock breakout measurement using the LIL VISAR. The VISAR interference fringes are initially static (the polish plane is immobile) and then suddenly disappear when the main shock propagating through the tube wall breaks out. A second shock due to hard x-ray preheating is also visible for targets with a thin tube wall ($e_{plane}$ = 10 µm). b) Example of VISAR signal obtained during this experiment with a thin gold wall ($e_{plane}$ = 10 µm) showing the change of target reflectivity relative to the VISAR laser probe due to the

"preheat shock" and the fringes disappearance when the "main shock" breaks out. The signal that lasts more than 10 ns is due to the reflection of the VISAR laser probe on a spatial fiducial. Scheme of the target illustrating how hard (keV) x-ray produced by the laser at the bottom of the spherical cavity can preheat the inner wall of the gold tube.

Figure 7 (a) and (b) show the measured breakout time of the "main shock" (green solid line), the "preheat shock" (blue solid line) and the coalesced shock (red solid line) as a function of the position z for two shots performed with an aerogel at density $\rho_0$ = 17.6 mg/cm$^3$ (gold wall thickness $e_{plane}$ = 10 µm) and $\rho_0$ = 39.4 mg/cm$^3$ (gold wall thickness $e_{plane}$ = 30 µm) respectively. The supersonic radiation front position already presented on Fig. 4 (b) is added (black solid lines) for comparison. Dotted lines are results from TROLL numerical simulations presented in section IV. The transit time of the shock, $\delta t_{transit}$, through the gold wall of thickness $e_{plane}$, is defined for a given position z as the delay between the time when the radiation front reaches this position z and the time when the "main shock" (or the coalesced shock) breaks out. As shown on Fig. 7 (a) and 7 (b), this time increases with the position z, which is attributed to a decrease of the ablation shock velocity due to the decrease of radiation temperature along the tube. On Fig. 7 (b), the "preheat shock" is not observed because of the large wall thickness ($e_{plane}$ = 30 µm) and only the breakout of the coalesced shock can be seen. The average velocity of the main shock in the gold wall is given by $V_{Au} = e_{plane} / \delta t_{transit}$. Assuming a steady ablation shock, its velocity can be linked to the drive temperature by $T_r \sim V_{Au}^{0.9}$ for gold in a large temperature range [150-500 eV].[28] In the case of a strong shock, reference [29] shows that $T_r \sim V_{Au}^{0.8}$. Below 150 eV, which corresponds here to the conditions of the drive temperature at the entrance of the gold tube, the shock velocity increases less quickly with the temperature and $T_r \sim V_{Au}^{1.9}$ [28]. The above expressions show that the decrease of $T_r(z)$ can then be estimated by measuring the transit time $\delta t_{transit}(z)$. Fig. 7 (c) represents the temperature $T_r(z)$ inferred using

the above expressions (solid lines). The amplitude of the temperature is constrained to be consistent with the maximum temperature (60±5 eV) at the exit of the tube determined from the broad-band x-ray spectrometer µDMX. Since µDMX performs spatially integrated measurement, the maximum radiation temperature represented on Fig. 7 (c) corresponds then to an average value over the tube diameter. Because of the limits of this simple model described above and the uncertainties on the wall thickness, µDMX error bars on the exit temperature and the uncertainties on the fit of the shock breakout and transit times of the radiation front in the process of inferring $T_r(z)$, are then taken into account to determine the error bars of this last quantity.

The same approach is used for the shot performed at $\rho_0 = 39.4$ mg/cm$^3$ where $e_{plane} = 30$ µm is thicker [see the grey solid line of Fig. 7 (c)]. The amplitude of the signal is here more difficult to constrain as µDMX diagnostic indicates that exit the temperature is below the detection threshold. Because of the geometry of the polished plane, no VISAR measurement is performed before z = 400 µm. Yet, that position is smaller than the effective x-ray photon mean free path $\lambda_{eff}$ in the medium at the entrance of the tube defined as $1/\lambda_{eff} = 1/\lambda_{Ross} + 1/\lambda_{geom}$ where $\lambda_{geom} = \phi_{tube}$ is the geometric photon mean free path.

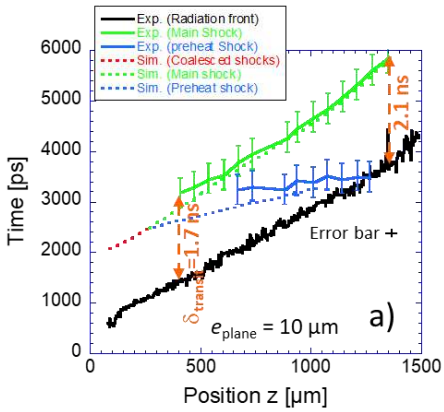


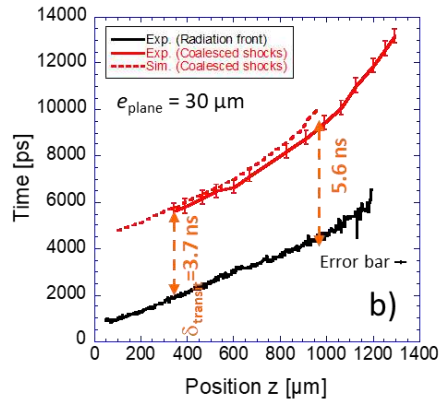


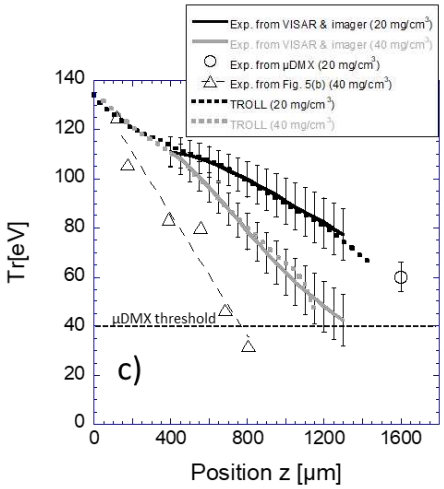

**FIG. 7.** Measured breakout time of the "main shock" (green solid line), the "preheat shock" (blue solid line) and the coalesced shock (red solid line) from the VISAR and radiation front trajectory from the soft x-ray imager (black solid line) as a function of the position z for shots performed with an aerogel at $\rho_0$ = 17.6 mg/cm$^3$ (a) and at $\rho_0$ = 39.4 mg/cm$^3$ (b). The crosses show the representative time and space error bar on the soft x-ray imager measurement. Dotted lines are results from TROLL simulations. c) Maximum average radiation temperature as a function of the longitudinal position z inferred from the VISAR and the soft x-ray imager measurement for these two shots (solid lines). µDMX exit temperature is added (disks). Maximum temperature inferred from Fig. 5(b) (triangles) (dashed line is a linear fit). Dotted lines correspond to TROLL simulation results.

Assuming that the radiation temperature profile along the tube can be written $T(x,t) \sim T_{S0}(t)[1-z/z_F(t)]^{1/(4+\alpha-\beta)}$,[15,16] this expression shows that for $\lambda_{eff}$ = 1070 µm at $\rho_0$ = 20 mg/cm$^3$ and $\lambda_{eff}$ = 630 µm at $\rho_0$ = 40 mg/cm$^3$, the maximum radiation temperature at z = 400 µm is almost identical for both aerogel densities. The amplitude of the solid grey line of Fig. 7(c) is then set so that at z = 400 µm, it is superimposed with the black solid line corresponding to the lower density case. The average maximum radiation temperature decreases faster along the tube at 39.4 mg/cm$^3$ than at 17.6 mg/cm$^3$ because of shorter photon mean free path. The decrease of radiation temperature seems to be rather linear for both densities. The triangles of Fig. 7(c) are extracted from Fig. 5(b) and correspond to the peak of the temporal profiles taken at different positions z along the tube. Data are normalized so that a linear fit tends toward the TROLL average entrance temperature of 135 eV. For that particular shot #4, the temperature fall is particularly quick compared to shot #1 for instance [see Fig. 5] and does not reproduce the temperature evolution inferred from the combined VISAR and soft x-ray imager measurements.

This behavior is likely due to pointing errors of the imager relative to the observation slit as discussed in section IV.

### D. WALL ALBEDO

Reference [18] presents an analytical model that explains the origin of bent Marshak wave propagating in low-density material enclosed in cylindrical tube. Bending is described as the consequence of x-ray energy losses at the tube wall because of its limited albedo, $a$, that tend to create a "drag" on the radiation front. The model gives the following expression for the radiation temperature structure:

$$\frac{T^4}{T_{S0}^4} = -\left(1+\frac{\varepsilon}{3}\right)cos\left(\sqrt{\varepsilon}\frac{y}{R}\right)\frac{sinh[k_0(z-zF)]}{\sinh(k_0 zF)} + \frac{4\varepsilon}{\pi}\sum_{n=1}^{\infty} cos(k_n y)\frac{(-1)^{n+1}}{n^2}\frac{sinh[k_n(z-zF)]}{\sinh(k_n zF)} \qquad (1)$$

where z is the longitudinal position (along the Marshak wave propagation direction), y the transverse position (perpendicular to the Marshak wave propagation direction), $z_F$ the front position at a given time, and $k_n = \{n\pi/2+[(n\pi/2)^2+\varepsilon]^{1/2}\}/R$ and $k_0 = \varepsilon^{1/2}/R$ are eigenvalues (n are integer values). $R$ is the tube radius and ε is a dimensionless parameter related to the wall albedo, $a$, by $\varepsilon = (3/4)\kappa\rho_0 R(1-a)$. As a reminder, κ corresponds to the material Rosseland mean opacity and $\rho_0$ to the material density. The position of the radiation front writes:

$$z_F = \frac{R}{\sqrt{\varepsilon}}cosh^{-1}\left(\frac{D\epsilon t}{2R^2}+1\right)cos\left(\sqrt{\varepsilon}\frac{y}{R}\right) + HOT \qquad (2)$$

where HOT are higher-order terms and $D=D_M(1+\varepsilon/3)$ is a modified radiation diffusion constant, $D_M=8\sigma T_{S0}^4/(3\kappa\rho_0 e)$ is the diffusion constant of Marshak wave and $\sigma = 1.03\times10^{-2}$ MJ/ns/cm$^2$. As a reminder, $e$ corresponds to the internal energy. Consequently, the transverse position of the radiation wave measured at the end of the tube, $z_f^{end}$ writes:

$$y_F(t) = \frac{R}{\sqrt{\varepsilon}}cos^{-1}\left(\frac{z_f^{end}}{\frac{R}{\sqrt{\varepsilon}}cosh^{-1}\left(\frac{D\epsilon t}{2R^2}+1\right)}\right) \qquad (3)$$

It is suggested in reference [18] that a fit of the radiation front position and shape with the above equations to infer parameters $D$ and ε should give access to the wall albedo $a$ using ε = (3/4)κρ$_0$$R$(1-$a$), assuming that the opacity κ is known. All these equations are written in a Cartesian coordinates and assume a constant drive temperature $T_{S0}$.

As the Marshak wave propagates inside a cylindrical tube in this experiment, it is natural to rewrite the above equations in cylindrical coordinates. Very similar expression are then obtained. The expression for the radiation temperature structure becomes:

$$\frac{T^4}{T_{S0}^4} = -\left(1+\frac{\varepsilon}{2}\right)J_0\left(\sqrt{2\varepsilon}\frac{r}{R}\right)\frac{sinh[k_0(z-zF)]}{\sinh(k_0 zF)} - 4\varepsilon\sum_{n=1}^{\infty}\frac{J_0(k_n r)}{\alpha_{1,n}^2 J_0(\alpha_{1,n})}\frac{sinh[k_n(z-zF)]}{\sinh(k_n zF)} \qquad (4)$$

where z is the longitudinal position (along the Marshak wave propagation direction), r the transverse radial position (perpendicular to the Marshak wave propagation direction), $z_F$ the front position at a given time. $J_0$ is the Bessel function of the first kind of order zero and $\alpha_{1,n}$ are the zeros of the Bessel function of the first kind of order one, $J_1$. Again, ε = (3/4)κρ$_0$$R$(1-$a$) and $k_n = \{\alpha_{1,n}/2+[(\alpha_{1,n}/2)^2+\varepsilon]^{1/2}\}/R$ and $k_0 = (2\varepsilon)^{1/2}$/R are eigenvalues. We make sure that $T^4/T_{S0}^4$ = 1 at z = r = 0 as $\sum_{n=1}^{\infty} 1/\alpha_{1,n}^2 J_0(\alpha_{1,n})$ = -1/8.

The position of the radiation front writes for a constant drive temperature $T_{S0}$:

$$z_F = \frac{R}{\sqrt{2\varepsilon}}cosh^{-1}\left(\frac{D\epsilon t}{R^2}+1\right)J_0\left(\sqrt{2\varepsilon}\frac{r}{R}\right) + HOT \qquad (5)$$

where $D$=$D_M$(1+ε/2) is still the modified radiation diffusion constant, $D_M$=8σ$T_{S0}^4$/(3κρ$_0$$e$) is the diffusion constant of Marshak wave. The transverse radial position of the radiation wave measured at the end of the tube, $z_f^{end}$ writes:

$$r_F(t) = \frac{R}{\sqrt{2\varepsilon}}J_0^{-1}\left(\frac{z_f^{end}}{\frac{R}{\sqrt{2\varepsilon}}cosh^{-1}\left(\frac{D\epsilon t}{R^2}+1\right)}\right). \qquad (6)$$

Since the drive temperature, $T_{S0}$, is not constant in our experiment, its evolution should be included in the above equations. Assuming it can be written $T_{S0}(t/t_0)^{\delta}$, Eq (5) becomes:

$$z_F = \frac{R}{\sqrt{2\varepsilon}}cosh^{-1}\left(\frac{D\epsilon t^{1+4\delta}t_0^{-4\delta}}{(1+4\delta)R^2}+1\right)J_0\left(\sqrt{2\varepsilon}\frac{r}{R}\right) \qquad (7)$$

and Eq (6) becomes:

$$r_F(t) = \frac{R}{\sqrt{2\varepsilon}} J_0^{-1}\left(\frac{Z_f^{end}}{\frac{R}{\sqrt{2\varepsilon}}cosh^{-1}\left(\frac{D\epsilon t^{1+4\delta}t_0^{-4\delta}}{(1+4\delta)R^2}+1\right)}\right). \qquad (8)$$

Figure 8 represents the predicted position of the leading edge of the radiation front as a function of time for $D_M$ = 0.49 mm²/ns, $R$ = 0.8 mm and two values of the small parameter ε. Results obtained using Eq (2) (black lines) derived in Cartesian coordinates for y = 0 were already presented in Figure 6 of reference [18]. They show how the energy losses at the tube wall (ε > 0) "drag" the radiation front compared to Marshak's solution (ε = 0). Gray lines correspond to new results obtained using Eq (5) derived in cylindrical coordinates for r = 0. They show identical results to the Cartesian case for ε = 0 corresponding to the classical Marshak's solution but a larger "drag" for ε = 0.3 when the effect of lossy wall is taken into account.

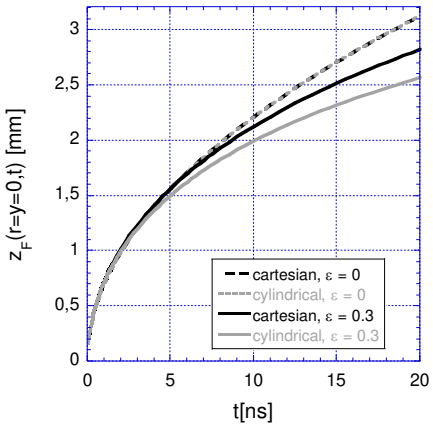


**FIG. 8.** Predicted position of the leading edge of the radiation front as a function of time for $D_M$ = 0.49 mm²/ns, $R$ = 0.8 mm and for ε = 0 (dotted and dashed lines) and ε = 0.3 (thick lines) (values from Fig. 6 of reference [18]). The black lines are obtained using Eq (2) derived

in Cartesian coordinates for y = 0 and the gray lines use Eq (5) derived in cylindrical coordinates for r = 0. Constant radiation temperature $T_{S0}$ is assumed here.

Figure 9 (a) and Fig. 9 (b) represent the measured (solid black lines) longitudinal position of the radiation front along the tube as a function of time, as already presented on Fig. 4(b), and its transverse position at the end of the tube as a function of time as already shown on Fig. 3(b) respectively for the low density case. These results are compared to fits of $z_F$ and $r_F$ using Eq (7) and Eq (8) where $R$ = 0.7 mm in this experiment. The measured time evolution of $z_F$ does not exhibit the classical square root evolution with time ($z_F \sim [\sigma T_{S0}^4 t/(\rho_0^2 \kappa e)]^{1/2}$ ) but is rather linear as the x-ray drive is not constant with time in this experiment [see Fig. 2]. This behavior is reproduced using $\delta = 0.4$. The diffusion constant $D_M$ is related to the radiation wave velocity, the larger this value, the larger the slope of $z_F$ with time [see Fig. 9(a)] and the earlier the breakthrough of the front for r = 0 at the end of the tube [see Fig. 9(b)]. The parameter $\varepsilon$ also plays on these two observables but mainly governs the measured curvature of the front at the end of the tube. Fits are obtained here with $\varepsilon = 0.6$ and $D_M = 1.25$ mm²/ns. Using $\varepsilon = (3/4)\kappa\rho_0 R(1-a)$ and $\kappa = 1/(gT^\alpha\rho^{-\lambda}) = 150$ cm²/g with the radiation temperature at the entrance of the tube $T_{S0}$ = 135 eV [see Fig. 7(c)] leads unfortunately to an unrealistic value of the wall albedo $a$. This is due to the fact that according to reference [18], an assumption needed for applicability of the theory is that $\rho\kappa R >> 1$ (the radial and z-direction need to be optically thick), which is not the case in our experiment conditions as $\rho\kappa R \sim 0.2$, which is in the wrong limit. The assumptions of the theory are not satisfied here.

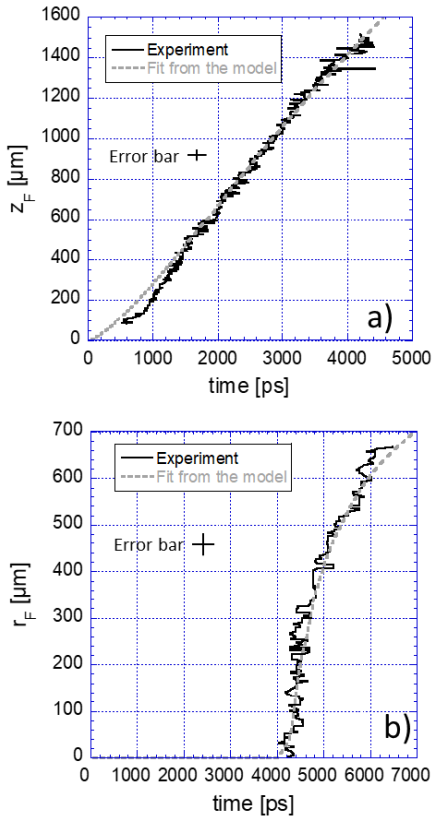


**FIG. 9.** Measure (solid black lines) longitudinal position (a) of the radiation front along the tube as a function of time from Fig. 4(b) and transverse position (b) at the end of the tube as a function of time from Fig. 3(b) compared to results from the model (grey dotted lines) using Eq (7) and Eq (8). Here, $R$ = 0.7 mm, $\rho_0$ = 20 mg/cm$^3$ and fits are obtained with $\delta$ = 0.4, $\varepsilon$ = 0.6 and $D_M$ = 1.25 mm²/ns. The crosses show the representative time and space error bar.

## IV. NUMERICAL SIMULATION RESULTS

Numerical simulations of the laser-produced radiation and shock fronts are performed with the 3D Lagrangian radiation-hydrodynamics code TROLL.[30] The simulations were

performed in the arbitrary lagrangian-eulerian (ALE) mode. Tabulated EOS (Equation Of State) and OPALV opacity[31] tables are used. Radiation transport is handled with an implicit Monte-Carlo (IMC), multigroup method. The simulation time is around 250 h with 512 processors on the Tera supercomputer at CEA-DIF.

Figure 10(a) shows a representation of the target used in the TROLL simulations. Targets are made of 2 million meshes including typically 100 meshes to describe the thickness of the wall with a geometric progression for their size (around 10 nm at the Au/$SiO_2$ aerogel interface). The spherical cavity, the tube filled with the $SiO_2$ aerogel and the cone can be seen, as well as the observation slit. Figure 10(b) show the radiation temperature of the target at different times. The expansion of the cavity plasma wall and the "bubble" of plasma produced by the LIL laser quadruplet irradiating the bottom of the spherical cavity can be seen. At late time, when the radiation front reaches the exit of the tube, the vacuum spherical gold cavity is eventually filled by plasma. At early time, the x-ray emission from the hot "bubble" of plasma produced an asymmetry drive at the entrance of the tube and the supersonic front is then not completely symmetric relative to the tube axis. A faster front propagation is observed off-axis. Later on, because of cavity thermalization and x-ray energy diffusion within the $SiO_2$ aerogel, the x-ray drive is no longer dominated by the "bubble" of plasma but rather by the thermal x-ray emission from the heated cavity wall, and the radiation front is then more axisymmetric. Note the curvature of the radiation front (also observed experimentally) that propagates faster on axis than near the tube wall because of x-ray energy losses at the wall.[18]

The inset image of Fig. 2 shows the radiation temperature of the target from the TROLL simulations. The x-ray emission seen by the broad-band x-ray spectrometer DMX comes mainly from the heated cavity LEH. Note that the cone shield also emits as it is also slightly heated by the laser energy contained in the focal spot at large radius (beyond the LEH). The measured laser focal spot shape was taken into account in the simulations. Simulated radiation

temperature is in agreement with measurement from DMX (no gold opacity multiplier wad used in the simulation).

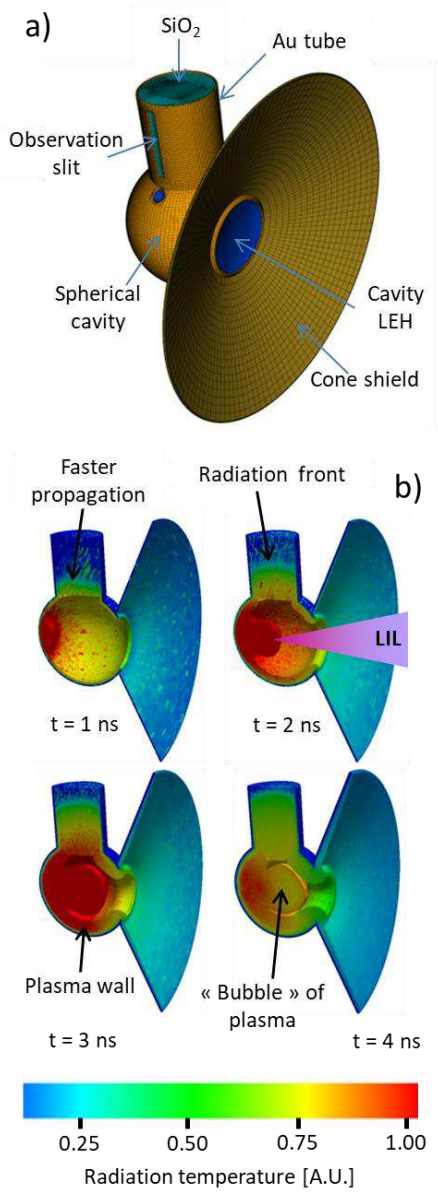

**FIG. 10** (a) 3D representation of the target used in TROLL simulations showing the spherical cavity with its protection cone. The observation slit of the gold tube filled with the $SiO_2$ aerogel is also visible. (b) Radiation temperature of the target from the TROLL simulations at different times.

The simulated temperature, $T_r = (D/R_{LEH})^{1/2}[F_{inc}/\sigma/\cos(\theta)]^{1/4}$, is inferred, as for the spectrometer DMX, by computing the incident x-ray flux, $F_{inc}$, (photon energy between 0 and 2 keV) from the LEH of radius $R_{LEH}$ on a detector positioned at a distance $D$ and at an angle of $\theta = 28°$ from the LEH. As a reminder, $\sigma$ is the Stefan-Boltzmann constant. This approach assumes that the LEH surface emits like a blackbody. The slight discrepancy between the simulated and measured cavity radiation temperature could be explained by laser beam pointing fluctuations as with a viewing angle of 28°, the broadband x-ray spectrometer can partially see the LIL quadruplet impact at the bottom of the cavity. Assuming a realistic 100 µm off-pointing of the quadruplet in a direction where the beam impact at the bottom of the cavity is more visible to DMX would then increase the incident flux, $F_{inc}$, in the above expression and bring the simulated radiation temperature history within the measured temperature error bars. Note also that as the radiation closure of the LEH was not measured, the simulated temperature [see Fig. 10(b)] may then also be too low if the radiation closure of the LEH is not correctly captured, with for instance a simulated LEH radius time evolution, $R_{LEH}(t)$, slower than in reality. The spherical cavity produces a relatively homogeneous x-ray flux on its wall. TROLL numerical simulations indicate that the x-ray flux entering the foam is similar to the x-ray flux emitted by the wall and seen by DMX up to 2 ns. Beyond that time, the flux entering the foam is affected by the radiation closure of the tube entrance [see Fig. 10(b)] and the associated radiation temperature is 3% lower than the DMX temperature at 3 ns.

### A. DYNAMICS OF THE SUPERSONIC RADIATION FRONT

Figure 11(a) is an inside view from the TROLL simulations of the tube wall and its observation slit which is affected by radiation closure, especially at the entrance of the tube where x-ray emission from the spherical cavity is more intense. Figure 11(b) is a simulation of the measurement from the soft x-ray imager (configuration #1) in the case where it is perfectly aligned on the slit. This simulation takes into account the spectral response of this diagnostic. The simulated results are qualitatively similar to what was measured [see Fig. 4(a)], the x-ray signal coming from the observation slit is reproduced. Figure 11(c) is similar to Fig. 11(b) but it shows the effect of a 40 μm (40% of the slit half-width) lateral pointing misalignment of the soft x-ray imager. The position of the supersonic radiation front is not affected by this misalignment, yet the signal amplitude is. The soft x-ray emission from the $SiO_2$ aerogel is here absorbed by the gold plasma expanding from the edge of the slit. The absorption is getting more and more important as the misalignment increases since the diagnostic line of sight is intercepted sooner by the gold plasma. Eventually, when the transverse misalignment reaches 100 % of the slit half-width, the absorption is total.

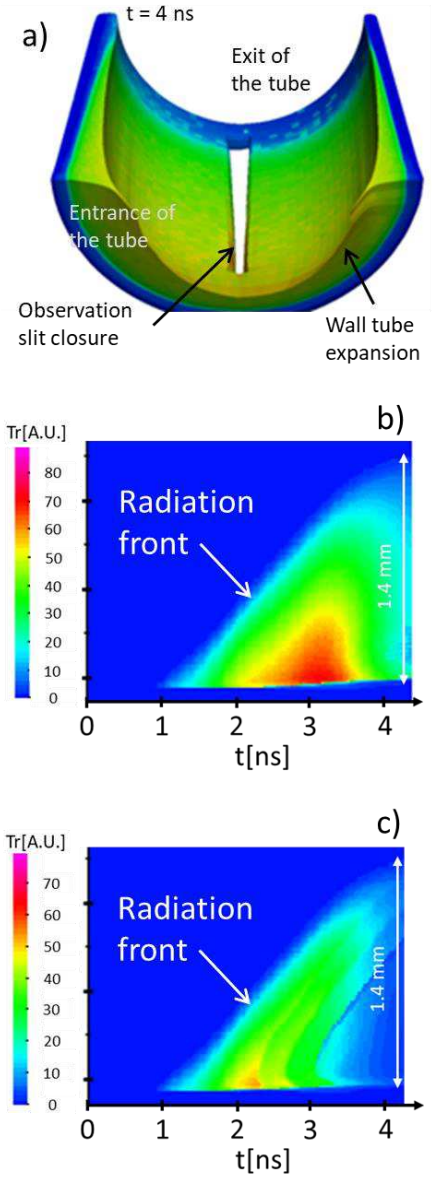

**FIG. 11** (a) Inside view of the gold tube from the TROLL simulations showing the radiation closure of the observation slit. Simulation of the soft x-ray imager data (b) when the imager is perfectly pointed on the slit, and (c) taking into account a 40 µm lateral off pointing.

The slit radiation closure affects the time of maximum emission for a given position z along the tube, yet the track of the radiation front (defined at the inflection point of radiation temperature temporal profiles) is not in our experimental conditions. Figure 4(b) show a comparison between measured (solid line) and simulated (dashed lines) transit times of the supersonic radiation front along the z direction of the tube for two aerogel densities (configuration #1). Simulations assume here a perfect pointing of the x-ray imager. An agreement to within 10% is obtained with measurement. The comparison for large density aerogel beyond z = 800 µm is more difficult as the signal from the soft x-ray imager is getting weak due to the temperature fall along the tube [see the inset image of Fig. 4(b)]. Fig. 3(b) shows that simulations of the front curvature at the end of the tube (configuration #2) is also close to measurement.

Figure 12 represents the TROLL simulated radiation front Mach number, $M$, as a function of the optical depth, $\tau$, obtained for the two aerogel densities tested in this experiment (green symbols). These results are compared to those from previous experiments summarized in Fig. 1 from reference [13] describing an experiment performed at the National Ignition Facility. The NIF experiment used $SiO_2$ aerogel or $C_8H_7Cl$ foam 3 mm long at a density around 120 mg/cm$^3$ driven by a peak radiation drive of 320 eV.

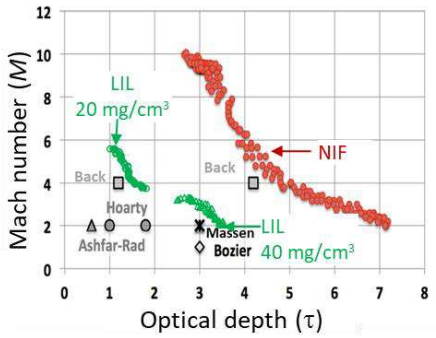


**FIG. 12** Radiation front Mach number, $M$, as a function of the optical depth, τ, from previous experiments (gray symbols) on supersonic radiation wave propagation extracted from reference [13] describing a NIF experiment (red symbols). The green symbols correspond to results from TROLL simulations describing the LIL experiment (for t > 1 ns after the spherical cavity radiation temperature sharp rise).

The large available laser energy (~ 350 kJ) for this NIF experiment allows working with a relatively high density and long medium, leading to large optical depth while remaining supersonic (red symbols). The LIL experiment was performed with a much lower laser energy (12 kJ) and x-ray drive (155 eV), yet a supersonic ($M$ > 2) and moderately diffusive (τ ≥ 1) regime of radiation front propagation is accessible for both foam densities.

### B. DECREASE OF THE RADIATION TEMPERATURE ALONG THE TUBE

Results from the VISAR measurement were also compared to TROLL simulations. TROLL simulated shock breakout time at the gold wall along the tube axis is represented by dotted lines on Fig. 7(a) in the case of the thin polished plane ($e_{plane}$ = 10 µm). Simulations show that at the entrance of the tube, the "main shock" produced by the radiation front and the "preheat shock" due to hard x-ray preheating are produced almost simultaneously and then coalesce within the wall before they break out at t ~ 2 ns. For t > 2.45 ns and position z > 250

μm, the "preheat shock" breaks out before the main shock. When the gold wall is chosen thick enough, both shocks coalesce within the tube wall whatever the position z and only the coalescence shock is observed [see Fig. 7(b)]. The measured shock breakout time is relatively well captured by hydrodynamic simulations.

Dotted lines of Fig. 7(c) show the maximum radiation temperature (averaged over the tube diameter similarly to the μDMX measurement) as a function of position z along the tube from TROLL simulations. Simulations show that the entrance temperature is 135 eV then it decreases with position z because of energies losses at the gold wall and losses to ionize and heat the aerogel. The temperature decreases more quickly at $\rho_0 = 39.4$ mg/cm$^3$ than at $\rho_0 = 17.6$ mg/cm$^3$. As the tube diameter is the same ($\phi_{tube}$ = 1400 μm) for both densities, x-ray energy losses at the tube wall are similar. The faster decrease of temperature at high density is mainly due to the shorter Rosseland mean free path. The increasing difference of radiation temperature along the tube between the two density cases, is also due to the fall of the input x-ray drive from the spherical cavity. At t = 4 ns for instance, the radiation front has already reached the exit of the tube at low density (20 mg/cm$^3$) whereas at large density (40 mg/cm$^3$), the front still has to propagates over several hundreds microns before reaching the exit. Consequently, as it is no longer supported, its temperature also falls. Results from numerical simulation also indicate that the assumption made on the maximum radiation temperature being almost identical at z = 400 μm for both aerogel densities is reasonable. The slight differences before z = 400 μm come from the experimental conditions (laser power and then cavity radiation temperature temporal profiles taken into account in the simulations) that can fluctuate from shot to shot.

## V. SUMMARY

The goal of this experiment performed on the Ligne d'Intégration Laser (LIL) facility was to study the propagation of a supersonic and moderately diffusive radiation front in low-density

$SiO_2$ aerogel in a gold tube driven by thermal radiation from a laser-heated spherical cavity. The front is studied along the tube by measuring its self-emission through an observation slit 200 µm wide using a 1D time resolved soft x-ray imager. The interest of this experimental configuration is that radiation front position can be studied continuously with time which is useful to better constrain analytical models or numerical simulations describing Marshak wave propagation, yet this configuration is also very sensitive to the observation slit radiation closure. If the propagation of the supersonic front can be studied, as it is fast enough not to be affected by this effect in our experimental conditions, its maximum temperature can't be correctly captured because of the closure. Experimental results are compared successfully to numerical simulations from the 3D Lagrangian radiation-hydrodynamics code TROLL that confirm the effect of closure on measurement, an effect that can even be exacerbated if one also includes pointing error (as low as 40 µm here corresponding to 40% of the slit half width) of the soft x-ray imager missing the center of the slit.

Radiation temperature along the tube was then inferred by combining results from the soft x-ray imager with those from a VISAR used to determine the average velocity of the ablation shock launched within the tube wall by the radiation front propagating inside the tube. Radiation temperature profile is also constrained by temperature measurement at the exit of the tube using the broadband x-ray spectrometer µDMX. This approach to study front temperature is new to our knowledge. Results show as expected that the inferred temperature decreases along the tube because of x-ray energy losses and that the decrease rate is larger for higher aerogel density.

**ACKNOWLEDGMENTS**

We acknowledge the support of experimental and target preparation staff of the LIL facility and staff of CEA/Valduc for target fabrication.

## DATA AVAILABILITY

The data that support the findings of this study are available from the corresponding author upon reasonable request.

## Author Contributions

**C. Courtois :** Conceptualization (equal); Formal Analysis (equal); Investigation (equal); Methodology (equal); Validation (equal); Visualization (equal); Writing/Original Draft Preparation (equal); Review & Editing (equal). **R. Gisbert :** Conceptualization (equal); Formal Analysis (equal); Investigation (equal); Methodology (equal); Validation (equal); Visualization (equal); Writing/Original Draft Preparation (equal); Review & Editing (equal). **O. Breton :** Investigation (equal); Resources; Review & Editing (equal). **S. Darbon :** Formal Analysis (equal); Investigation (equal); Resources (equal); Validation (equal); Review & Editing (equal). **J. Fariaut :** Formal Analysis (equal); Investigation (equal); Resources (equal); Validation (equal); Review & Editing (equal). **O. Henry :** Formal Analysis (equal); Investigation (equal); Validation (equal); Review & Editing (equal). **D. Raffestin :** Formal Analysis (equal); Investigation (equal); Validation (equal); Review & Editing (equal). **C. Reverdin :** Formal Analysis (equal); Investigation (equal); Resources (equal); Validation (equal); Review & Editing (equal). **G. Soullie :** Formal Analysis (equal); Investigation (equal); Resources (equal); Validation (equal); Review & Editing (equal). **B. Villette :** Formal Analysis (equal); Investigation (equal); Resources (equal); Validation (equal); Review & Editing (equal).

**References**

[1]D. Mihalas and B. W. Mihalas, Foundations of Radiation Hydrodynamics (Oxford University Press, New York, 1984).

[2]V. Tranchant, N. Charpentier, L. Van Box Som, A. Ciardi, and É. Falize, The Astrophysical Journal, **936**, 14 (2022).

[3]J. Lindl, Physics of Plasmas **2**, 3933 (1995). J. D. Lindl, P. Amendt, R. L. Berger, S. G. Glendinning, S. H. Glenzer, S. W. Haan, R. L. Kauffman, O. L. Landen and L. J. Suter, Physics of Plasmas **11**, 339 (2004).

[4]J. Garnier, G. Malinié, Y. Saillard, and C. Cherfils-Clérouin, Phys. Plasmas **13**, 092703 (2006).

[5]D. Hoarty, O. Willi, L. Barringer, C. Vickers, W. Nazarov, Phys. Plasmas **6**, 2171(1999).

[6]C. Courtois, C. Robert, D. Bretheau, J. Fariaut, M. Ferri, I. Geoffray, G. Legay, F. Philippe, R. Rosch, G. Soullie, and B. Villette, Phys. Plasmas **28**, 073301 (2021).

[7]T. Afshar-rad, M. Desselberger, M. Dunne, J. Edwards, J. M. Foster, D. Hoarty, W. Jones, S. J. Rose, P. A. Rosen, R. Taylor, and O. Willi, Phys. Rev. Lett. **73**, 74 (1994).

[8]J. Massen, G. D. Tsakiris, K. Eidmann, I. B. Foldes, T. Lower, R. Sigel, S. Witkowski, H. Nishimura, T. Endo, H. Shiraga, M. Takagi, Y. Kato, and S. Nakai, Phys. Rev. E **50**, 5130 (1994).

[9]C. A. Back, J. D. Bauer, J. H. Hammer, B. F. Lasinski, R. E. Turner, P. W. Rambo, O. L. Landen, L. J. Suter, M. D. Rosen, and W. W. Hsing, Phys. Plasmas **7**, 2126 (2000); C. A. Back, J. D. Bauer, O. L. Landen, R. E. Turner, B. F. Lasinski, J. H. Hammer, M. D. Rosen, L. J. Suter, and W. H. Hsing, Phys. Rev. Lett. **84**, 274 (2000).

[10]C. Constantin, C. A. Back, K. B. Fournier, G. Gregori, O. L. Landen, S. H. Glenzer, and E. L. Dewald, Phys. Plasmas **12**, 063104 (2005).

[11]Y. Xu, S. Jiang, D. Lai, W. Pei, Y. Ding, T. Chang, K. Lan, S. Li, and T. Feng, Laser Part. Beams **24**, 495 (2006).

[12]P. Keiter, M. Gunderson, J. Foster, P. Rosen, A. Comley, M. Taylor, and T. Perry, Phys. Plasmas **15**, 056901 (2008).

[13]A. S. Moore, T. M. Guymer, J. Morton, B. Williams, J. L. Kline, N. Bazin, C. Bentley, S. Allan, K. Brent, A. J. Comley, K. Flippo, J. Cowan, J. M. Taccetti, K. Mussack-Tamashiro, D. W. Schmidt, C. E. Hamilton, K. Obrey, N. E. Lanier, J. B. Workman, and R. M. Stevenson, J. Quant. Spectrosc. Radiat. Transfer **159**, 19 (2015).

[14]T. M. Guymer, A. S. Moore, J. Morton, J. L. Kline, S. Allan, N. Bazin, J. Benstead, C. Bentley, A. J. Comley, J. Cowan, K. Flippo, W. Garbett, C. Hamilton, N. E. Lanier, K. Mussack, K. Obrey, L. Reed, D. W. Schmidt, R. M. Stevenson, J. M. Taccetti, and J. Workman, Phys. Rev. Lett. **22**, 043303 (2015).

[15]J.H. Hammer and M. D. Rosen, Phys. Plasmas **10**, 1829, (2003).

[16]A.P. Cohen, G. Malamud, and S.I. Heizler, Phys. Rev. Research **2**, 023007 (2020).

[17]H.M. Johns, C.L. Fryer, S.R. Wood, C.J. Fontes, P.M. Kozlowski , N.E. Lanier, A. Liao, T.S. Perry, J.W. Morton, C.R.D. Brown, D.W. Schmidt, T. Cardenas, T.J. Urbatsch, P. Hakel, J. Colgan, S. Coffing, J. Cowan, D. Capelli, L.A. Goodwin, T.E. Quintana, C. Hamilton, F. Fierro, C. Wilson, R.B. Randolph, P. Donovan, T. Sedillo, R. Gonzales, M.E. Sherrill, M.R. Douglas, W.J. Garbett, J.D. Hager, J. Kline, High Energy Density Phys. **39** 100939 (2021).

[18]O. A. Hurricane and J. H. Hammer, Phys. Plasmas **13**, 113303 (2006).

[19]Z. Ji-Yan, Y. Jia-Min, J. Shao-En, L. Yong-Sheng, Y. Guo-Hong, D. Yao-Nan, H. Yi-Xiang, and H. Xin, Chin. Phys. B **19**(2), 025201 (2010).

[20]L Videau, E Alozy, I Bailly, N Borisenko, J Y Boutin, J Breil, S Brygoo, M Casanova, A Casner, L Chauvel, C Chenais-Popovics, C Courtois, S Darbon, S Depierreux, J M Di-Nicola, P Di-Nicola, F Durut, A Duval, J Ebrardt, J L Feugeas, C Fourment, S Gary, J C Gauthier, M Grech, O Henry, A Herve, S Hulin, S Huller, G Huser, J P Jadaud, F Jequier, Ch Labaune, J Limpouch, P Loiseau, O Lutz, P H Maire, M Mangeant, C Meyer, D T Michel, J L Miquel, M

C Monteil, M Naudy, W Nazarov, Ph Nicolai, O Peyrusse, F Philippe, D Raffestin, C Reverdin, G Riazuello, Ph Romary, R Rosch, C Rousseaux, G Soullie, S Schmitt, G Schurtz, Ch Stenz, V Tassin, F Thais, C Thessieux, G Thiell, M Theobald, V Tikhonchuk, J L Ulmer, B Villette, F Wagon and R Wrobel, A. C. Machacek, J. S. Wark, R. Allott, R. J. Clarke, and P. A. Norreys, Plasma Phys. Control. Fusion **50**, 124017 (2008).

[21]J. L. Bourgade, B. Villette, J.L. Bocher, J.Y. Boutin, S. Chiche, N. Dague, D. Gontier, J. P. Jadaud, B. Savale and R. Wrobel, Rev. Sci. Instrum. 72, 1173 (2001). J. L. Bourgade, V. Allouche, J. Baggio, C. Bayer, F. Bonneau, C. Chollet, S. Darbon, L. Disdier, D. Gontier, M. Houry, H. P. Jacquet, J. P. Jadaud, J. L. Leray, I. Masclet-Gobin, J. P. Negre, J. Raimbourg, B. Villette, I. Bertron, J. M. Chevalier, J. M. Favier, J. Gazave, J. C. Gomme, F. Malaise, J. P. Seaux, V. Yu Glebov, P. Jaanimagi, C. Stoeckl, T. C. Sangster, G. Pien, R. A. Lerche, and E. R. Hodgson, Rev. Sci. Instrum. **75**, 4204 (2004). J. P. Le Breton, E. Alozy, J. Y. Boutin, A. Duval, S. Gary, D. Gontier, S. Jasmin, M. Naudy, C. Reverdin, R. Rosch, S. Schmitt, G. Soullie, P. Stemmler, B. Villette, R. Wrobel, S. Hulin, C. Meyer, and P. Romary, Rev. Sci. Instrum. **77**, 10F530 (2006).

[22]R. Rosch, J. Y. Boutin, J. P. Le Breton, D. Gontier, J. P. Jadaud, C. Reverdin, G. Soullié, G. Lidove, and R. Maroni, Rev. Sci. Instrum. **78**, 033704 (2007).

[23]L.M. Barker, R.E. Hollenbach, J. Appl. Phys. **43**, 4669 (1972).

[24]P.M. Celliers, D.K. Bradley, G.W. Collins, D.G. Hicks, T.R. Boehly, W.J. Armstrong, Rev. Sci. Instrum. **75**, 4916 (2004).

[25]S. Darbon, A. Duval, I. Masclet-Gobin, B. Marchet, S. Brygoo, C. Courtois, G. Debras, L. Patissou, R. Parreault, O. Lobios, M. Mangeant, S. Parrot and O. Hartmann, IFSA 2011 - Seventh International Conference on Inertial Fusion Sciences and Applications, Bordeaux, France, EPJ Web of Conferences **59**, 13001 (2013).

[26]C. Courtois, O. Poujade, E. Alozy, S. Brygoo, C. Chicanne, T. Chies, S. Darbon, A. Duval, J. Fariaut, M. Ferri, H. Graillot, O. Henry, B. Marchet, I. Masclet-Gobin, P. Seytor, G. Soullie, L. Videau, B. Villette, and R. Wrobel, Phys. Plasmas 27, 042702 (2020).

[27]J. Massen, G. D. Tsakiris, K. Eidmann, I. B. Foldes, Th. Lower, R. Sigel, S. Witkowski, H. Nishimura, T. Endo, H. Shiraga, M. Takagi, Y. Kato and S. Nakai, Phys. Rev. E **50**, 5130 (1994).

[28]G. Mishraa, K. Ghosha, A. Raya, N.K. Gupta, High Energy Density Phys. **27** 1 (2018).

[29]T. Shussman and S. I. Heizler, Phys. Plasmas 22, 082109 (2015).

[30]E. Lefebvre, S. Bernard, C. Esnault, P. Gauthier, A. Grisollet, P. Hoch, L. Jacquet, G. Kluth, S. Laffite, S. Liberatore, I. Marmajou, P.-E. Masson-Laborde, O. Morice and J.-L. Willien, Nucl. Fusion **59**, 032010 (2019).

[31]F.J.D. Serduke, E. Minguez, S.J. Davidson, C. A. Iglesias, JQSRT **65**, 527 (2000).

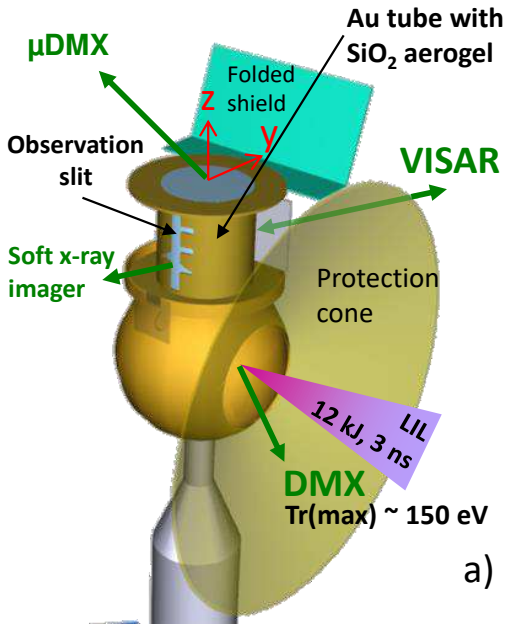


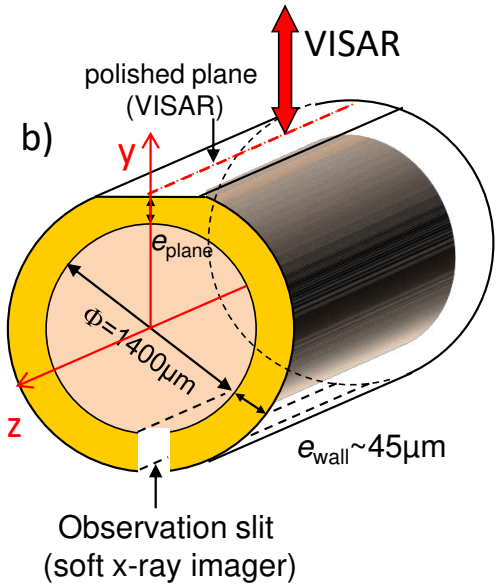


Courtois – Fig.1

Courtois – Fig.2

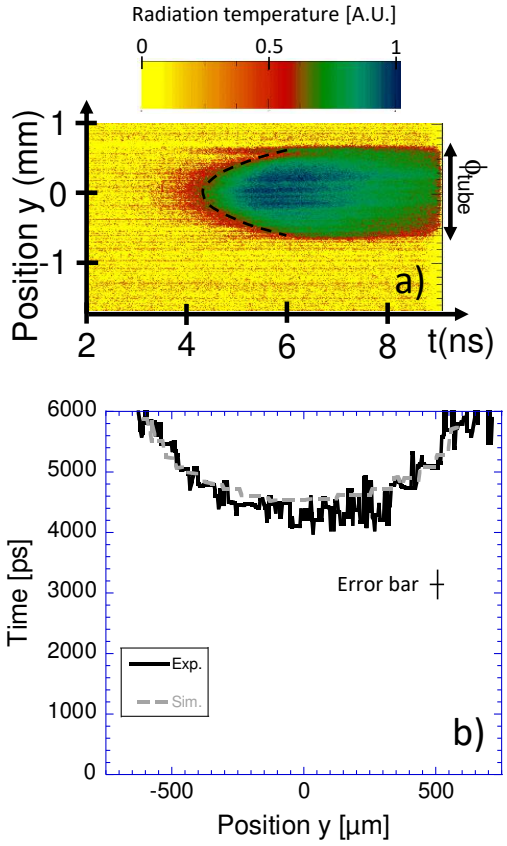


Courtois – Fig.3

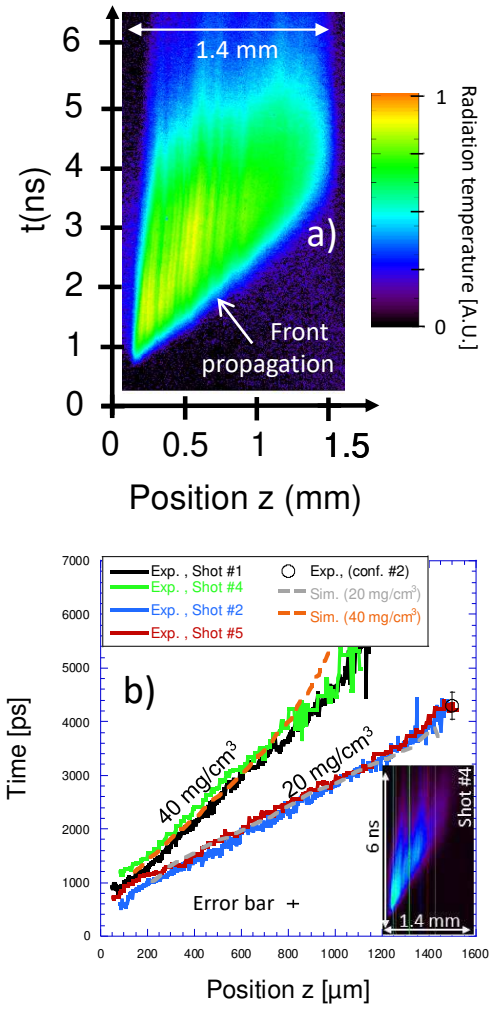


Courtois – Fig.4

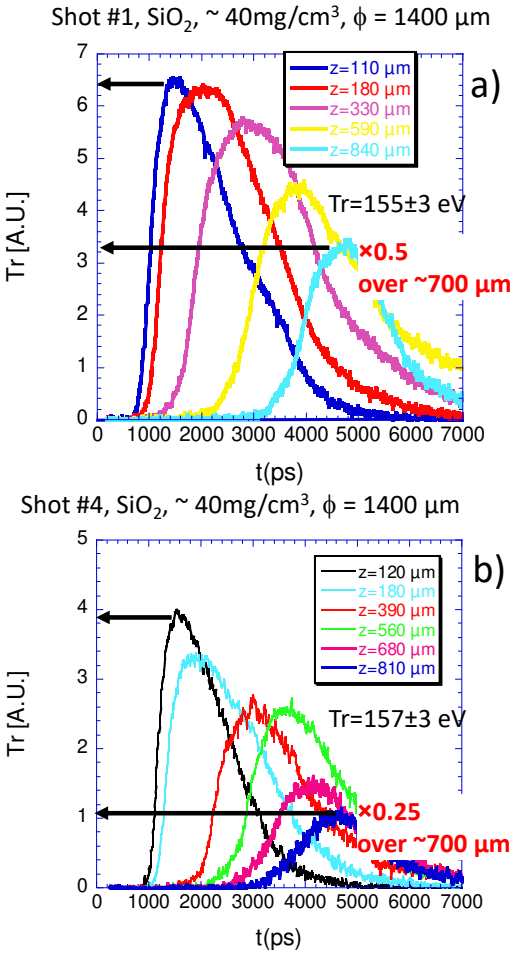


Courtois – Fig.5

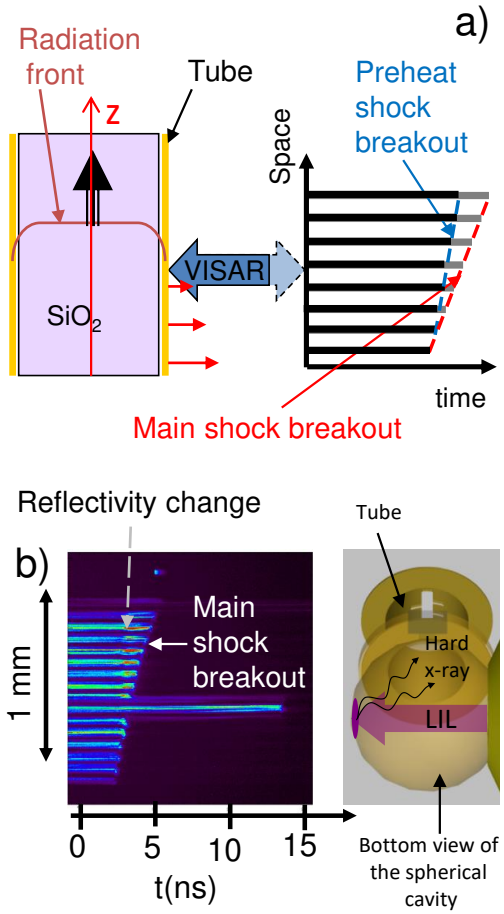


Courtois – Fig.6

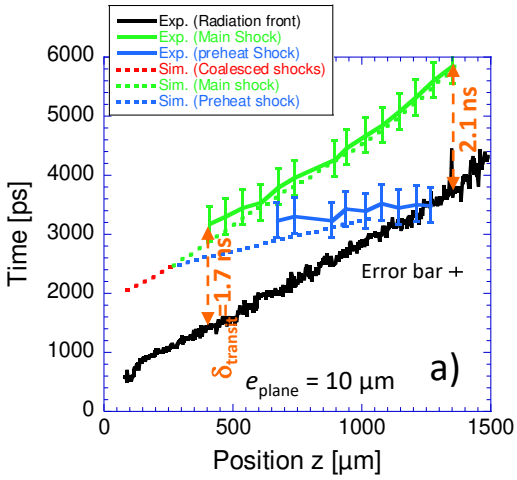


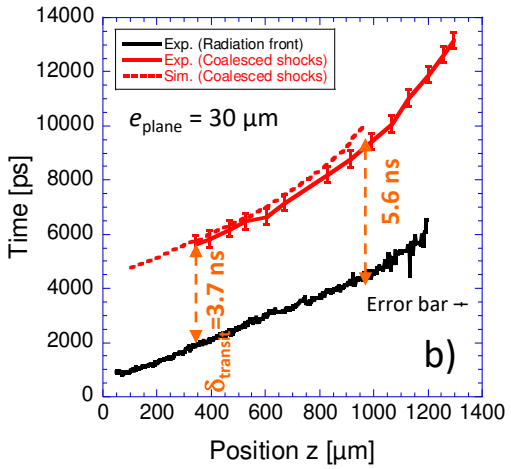


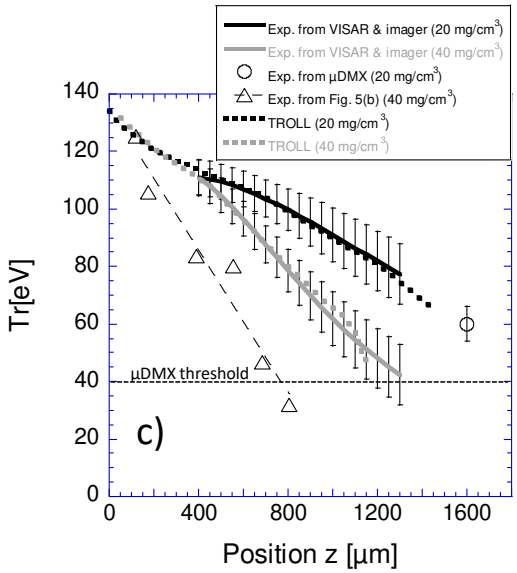


Courtois – Fig.7

Courtois – Fig.8

Courtois – Fig.9

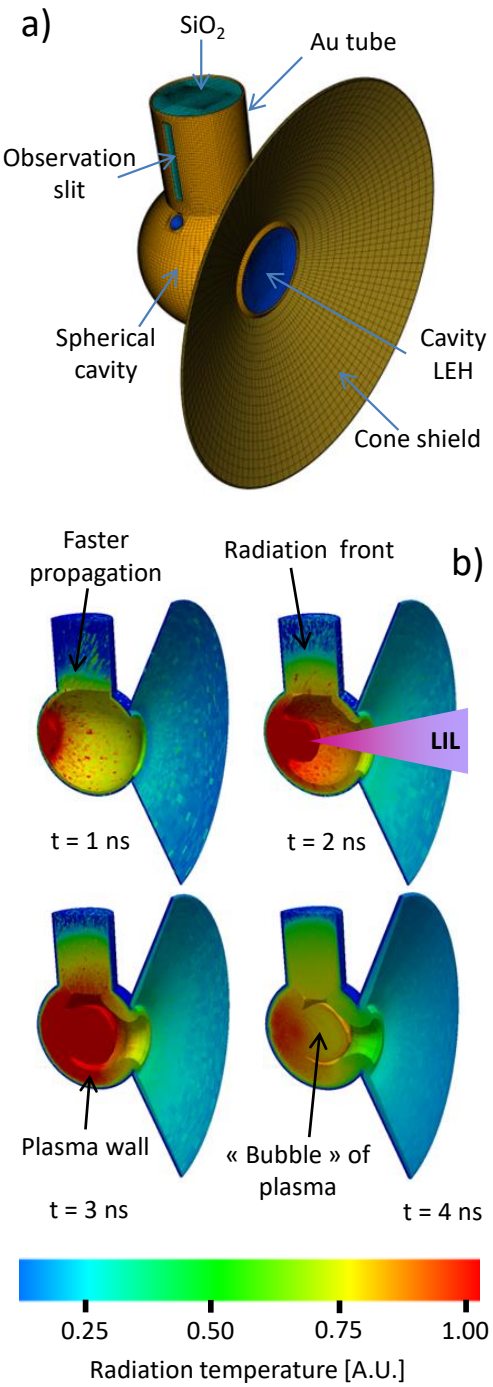


Courtois – Fig.10

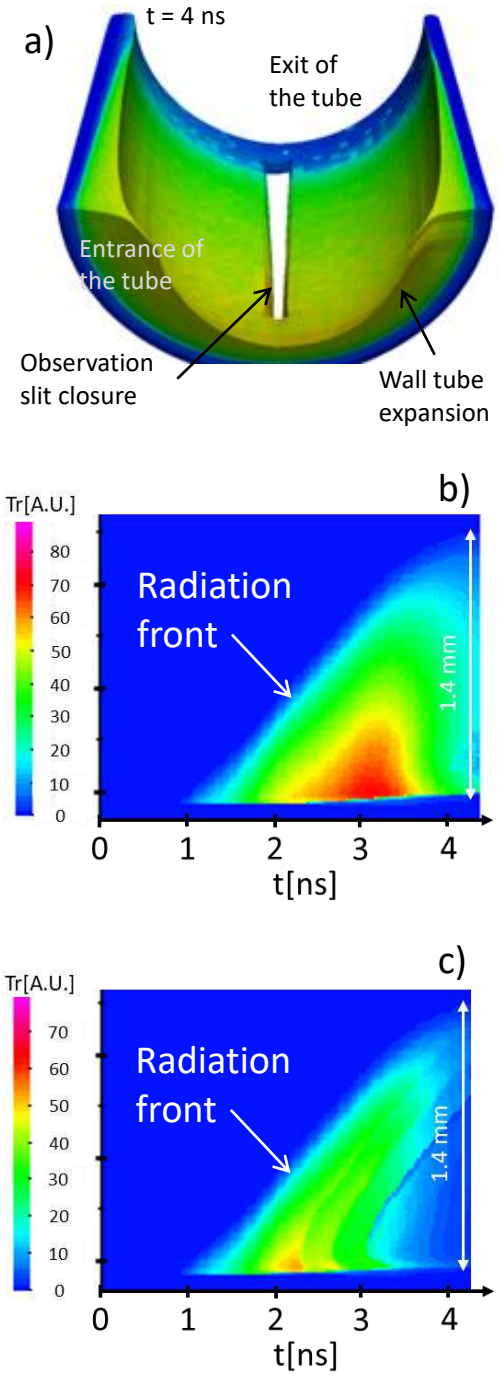


Courtois – Fig.11

Courtois – Fig.12